

Space-based passive orbital manoeuvre detection algorithm via a new characterization

Baichun Gong^{*†}, Xin Jin^{*}, Linhai Jiang^{*}, and Mo Ren[§]

^{*} *Nanjing University of Aeronautics and Astronautics
29 Jiangjun Rd, Nanjing 210016, China*

[§] *Equipment Department of the Space System Division*

baichun.gong@nuaa.edu.cn

[†] Corresponding Author

Abstract

Orbital manoeuvre detection for non-cooperative targets is a key task in space situational awareness. This study develops a passive manoeuvre detection algorithm using angles measured by a space-based optical sensor. Emphasis is placed on constructing a new characterization for manoeuvres as well as the corresponding detection method, especially for targets in high-altitude orbit, the relative distance between vehicles is far less than their geocentric distance. First, the concept of relative angular momentum is introduced to characterize the orbital manoeuvre of the target quantitatively. Second, a detection algorithm is designed where sliding windows and correlations are utilized to determine the mutation of the manoeuvre characterization. Lastly, the proposed algorithm is verified through numerical simulations.

1. Introduction

With the rapid development of space technology, the frequency of launching satellites in various countries has increased rapidly. For example, SpaceX plans to launch 42,000 satellites for Starlink. The huge number of launches may have disastrous consequences for near-Earth space [1-5]. The falling off of objects produced in the launch process, failed satellites at the end of their service life or after failure may affect the normal operation of active satellites or even cause collisions. Collisions and secondary collisions will produce countless space debris, which is very difficult to remove and poses a major threat to the safety of satellites [6-9]. In addition, the mastery of space requires huge national interests. Space provides an important support for national security. Fierce competition in space utilization technology has occurred, which makes the importance of space security increasingly prominent [9-11]. Therefore, to protect space resources, whether to avoid damage caused by space debris or to defend against space military threats, it is extremely critical to improve space situational awareness.

To date, many situational awareness methods have been proposed. Based on the environment in which the measuring equipment is located, existing situational awareness methods can be divided into space-based awareness and ground-based awareness methods. The main method of ground-based sensing establishes an observation station on the ground, and the operational state of the target is observed using ground-based radar and photoelectric systems [12-15]. The effectiveness of ground-based methods has been confirmed; for example, the U.S. Army has operated approximately 30 ground-based space situational awareness systems [12]. These systems can effectively observe hundreds of different targets every day, but there are also some problems with ground-based methods. First, owing to the influence of geographical geometric factors, the observation range of a single observation station is very limited. Plus, the alternation of day and night also has a negative impact on the observation of some equipment requiring optical information, which also makes it difficult for ground-based situational awareness systems to achieve an all-weather observation capability. This problem can be solved by deploying ground observation stations worldwide. For example, the ground-based sensing system of the United States is distributed in the United States, Great Britain, Norway, the Atlantic, the Indian Ocean, the Pacific, and other places. However, this solution is not only constrained by political factors, but also has the problems of high construction costs and complex maintenance. Therefore, increasing attention has been paid to research focusing on space-based situational awareness.

Space-based methods can overcome many of the shortcomings of ground-based methods, such as direct observation of space targets in space can overcome the influence of the atmosphere and the limitation of the field of regard. The deployment of space-based assets in shared space also overcomes the need to deploy stations in other countries. At

present, researchers have proposed many space-based sensing methods. Several space-based sensing systems have been used in practical applications, like the MiTEx satellite of the United States [16], the GSSAP project [16-18] and the ESPASat platform [19].

Sensors for space-based sensing generally include lidar, radio ranging equipment, and optical cameras [16-24]. Among space-based navigation methods, the optical angle-only navigation method has become the prominent development trend because of its relatively simple equipment and high reliability [21-24]. The angle-only navigation method only needs to perceive the relative geometric properties of the chaser satellite and target satellite to determine the orbit of the target satellite. Considering the related measurement errors in practical applications, the Kalman filter method is the most commonly introduced to deal with the errors in measurement. However, the traditional Kalman filter method can only deal with known perturbations and common measurement errors such as biases, scale-factors and noise. When the target satellite performs unknown orbit manoeuvres due to collisions, perturbations, or orbit changes, the orbit determination error often diverges gradually over time. Therefore, navigation based on this method will lose its effectiveness in these cases. To solve this problem, it is necessary to find a way to detect the orbit manoeuvre and estimate the manoeuvre time.

Researchers have studied orbit manoeuvre detection from multiple angles. Some studies have started with improving the navigation accuracy or data processing methods [25-30]. For example, Jia et al. [25] proposed an improved Kalman filter algorithm using four cooperative satellites, which could achieve the goal of detecting the target orbit manoeuvre accurately, but the cost increases a lot, like for more individual cooperation or the high cost of high-precision sensors. Previous studies [26-27] proposed empirical mode decomposition (EMD) processing for the detected quantity, which allowed the abnormal points of parameters to be highlighted among the observed values to realize the identification of manoeuvres or abnormal points. Scientists have proposed these methods because the state parameters of general space targets, such as velocity and position, are not sensitive to orbit manoeuvres, and their changes caused by orbit manoeuvres are easily submerged in measurement errors, particularly for long-range targets. Therefore, identifying new feature quantities that are sensitive to manoeuvres is a new trend in this field [31-36]. For example, Yu et al. and Huang et al. [31-32] proposed the use of the semi-major axis and eccentricity as detection quantities for manoeuvres, but these quantities have certain limitations in the use scenarios. [33] proposed a manoeuvring weighted fusion of multi hypothesis tests (WFMHT) method for space-based angle-only measurement, in which the observation error in the Extended Kalman Filter calculation was set as the characterization, and target manoeuvres were determined by judging whether the residual had the characteristics of zero-mean white noise. The method proposed by [13] used the orbit determination residual to evaluate the start and end times of manoeuvres. [34] proposed using the calculated rate of change in the distance as the characterization and transformed the orbit manoeuvre detection problem into a hypothesis test problem. Although these methods are valuable, they all have certain application limitations. Some are not suitable for small orbit manoeuvre detection, whereas others have poor real-time performance or some limitations.

In conclusion, to solve the problem of orbit manoeuvre detection based on passive optical angle-only measurements in the field of space-based sensing, this study constructs a new characterization and proposes an orbit manoeuvre detection method based on it. The proposed method can detect the orbit manoeuvres of long-range targets a relatively simple filtering algorithm and is also applicable to close-range targets.

The rest of the manuscript is organized as follows. Following the problem statement in Section 2, the model of the manoeuvring characterization and its sensitivity analysis are presented in Section 3. The manoeuvre detection algorithm is addressed in Section 4. The numerical simulation framework is described in Section 5. The results of the simulations and analysis are presented in Section 6. Finally, conclusions are given in Section 7.

2. Problem statement

Based on space-based observation, the target's line-of-sight angle is measured to provide a continuous evaluation of whether the target is performing an orbital manoeuvre, and the orbital manoeuvring time is estimated. The logic framework of the continuous detection algorithms is given in Section 2.1, and the kinematic model used in this study is introduced in Section 2.2; finally, the measurement model of the target line-of-sight angle is introduced in Section 2.3.

2.1 Framework of the manoeuvre detection algorithm based on angle-only measurements

The basic logical relationship of the non-cooperative target orbit manoeuvre angle-only detection method proposed in this study is shown in Fig. 1. First, the line-of-sight angle measurement is filtered and estimated in combination with the dynamic model to obtain the relative orbit parameters of the non-cooperative target. Then, the manoeuvre-detecting characterization is constructed based on the relative orbit parameters. Finally, the manoeuvre time is determined through the inspection and discrimination of the characterization, and the process of determining of the initial orbit is restarted at the same time.

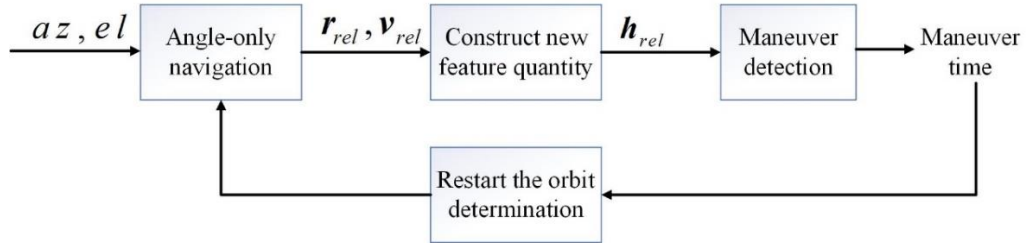


Figure 1: Framework of the algorithm

Because the focus of this study is the design of the manoeuvre detection algorithm, the angle measurement and orbit determination algorithm including the filter in Fig. 1 is not discussed in detail, and the method proposed by Gong et al. [37] is adopted directly. The mapping relationship between the history of line-of-sight angle and the relative orbit parameters is given as follows:

$$\begin{bmatrix} \mathbf{r}^T, \mathbf{v}^T \end{bmatrix}^T = \text{Mapping}(az, el) \quad (1)$$

where az and el are the history of the azimuth and elevation, respectively.

2.2 Relative motion dynamics model

As shown in Fig. 2, a rotating frame, i.e., a local vertical local horizontal (LVLH) reference coordinate system, is established. The origin is located at the center-of-mass (COM) of the chaser satellite, the X-axis points to the COM of the satellite from the Earth's center, the Z-axis is normal to the orbital plane, and the Y-axis completes the right-hand system.

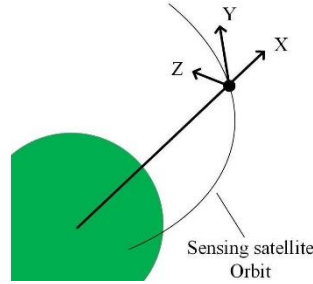


Figure 2: LVLH reference system

When the orbital eccentricity e , of the two satellites satisfies $0 \leq e < 1$, the nonlinear relative dynamics model proposed by Yamanaka et al. [38] can be used to model the relative state between the chaser satellite and the target satellite:

$$\begin{bmatrix} \ddot{x} \\ \ddot{y} \\ \ddot{z} \end{bmatrix} = \begin{bmatrix} -k\omega^2 x + 2\omega\dot{z} + \dot{\omega}z + \omega^2 x \\ -k\omega^2 y \\ 2k\omega^2 z - 2\omega\dot{x} - \dot{\omega}x + \omega^2 z \end{bmatrix} + \mathbf{a}_f + \mathbf{a}_{cd} - \mathbf{a}_{td} \quad (2)$$

where $[x, y, z]^T$ is the position of the target's COM relative to the COM of the chaser satellite in LVLH frame, ω is the orbital angular velocity of the chaser satellite, \mathbf{a}_f is the acceleration caused by the propulsion force of the target satellite, \mathbf{a}_{cd} is the acceleration caused by forces other than the inverse square gravity term on the chaser satellite, and \mathbf{a}_{td} is the acceleration caused by forces other than the inverse square gravity term on the target satellite. The constant k is defined as follows:

$$k \cong \frac{\mu}{h^{3/2}} \quad (3)$$

where μ is the gravitational constant, and h is the orbital angular momentum.

In this paper, we assume the chaser satellite is flying in free motion and the external forces on the chaser satellite and the target satellite are identical

$$\mathbf{a}_f = \mathbf{0}, \quad \mathbf{a}_{cd} = \mathbf{a}_{td} \quad (4)$$

2.3 Measurement model

In this study, it is assumed that the orbit and attitude of the chaser satellite are known, and only passive optical cameras on the satellite can be used to measure non-cooperative targets. According to the engineering constraints, the camera is installed away from the satellite centroid, and the measurement is shown in Fig. 3. Therefore, the measurement model of the azimuth and elevation can be established directly in the LVLH system:

$$\begin{cases} az_i = \tan^{-1} \left(\frac{z - d_z}{y} \right) + n_1 \\ el_i = \tan^{-1} \left(\frac{x - d_x}{\sqrt{(y - d_y)^2 + (z - d_z)^2}} \right) + n_2 \end{cases} \quad (5)$$

where $[x, y, z]^T$ is the relative position vector of the target at t_i , $[d_x, d_y, d_z]^T$ is the installation position vector of the camera offset from the COM of the chaser satellite, and $[n_1, n_2]^T$ is the measurement noise.

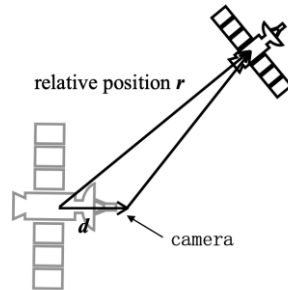


Figure 3: Diagram of offset camera measurement

The offset of the camera can increase the observability of relative orbit if the offset satisfies the observable criterion. As well, the increment of observability depends on the ratio of the effective offset to the relative range between two spacecraft. Detailed analysis for the angles-only observability from the offset can be found in a study by Gong et al. [37].

3. Modelling of the manoeuvring characterization

As analysed in Section 1, the existing algorithms that use the features such as semi-major axis and eccentricity to detect the orbit manoeuvre suffer from poor sensitivity in many applications, especially in the cases of high-altitude orbit, e.g. GEO. Therefore, a new manoeuvre detection feature based on the concept of relative angular momentum is proposed for high-altitude orbit cases in this study. The following sections describe the definition of the characterization to be tested.

In this study, it is assumed that the orbit and attitude of the chaser satellite are known, and only passive optical cameras on the satellite can be used to measure non-cooperative targets. According to the engineering constraints, the camera

is installed away from the satellite centroid, and the measurement is shown in Fig. 3. Therefore, the measurement model of the azimuth and elevation can be established directly in the LVLH system:

The relative angular momentum is defined as follows:

$$\mathbf{h}_{rel} = \mathbf{r}_{rel} \times \mathbf{v}_{rel} \quad (6)$$

where $\mathbf{r}_{rel} = [x, y, z]^T \in \mathbb{R}^3$, $\mathbf{v}_{rel} = [\dot{x}, \dot{y}, \dot{z}]^T \in \mathbb{R}^3$.

A manoeuvre directly affects the position and velocity vectors of the satellite, and the calculation of the angular momentum is related to the position and velocity vector of the object [6]. The cross product of relative position and velocity vectors can not only reflect the changes in the values of relative position and relative velocity, it can also directly reflect the changes in the direction of the relative position and relative velocity through the change in the value of the angular momentum, which makes the relative angular momentum more sensitive to satellite manoeuvres than Individual velocity or position. In a very short time after manoeuvre, the value of position is large comparing to velocity, but its change is close to zero, the value of velocity and of its change are both very small. Relative angular momentum amplifies the change of velocity by cross product of velocity and position, so that its change is easier to be detected than that of velocity. Compared with the position almost unchanged in a very short time after manoeuvre, the relative angular momentum has more obvious changes because of the implicit velocity information, so it is easier to be detected. In addition, using the relative angular momentum as characterization to detect manoeuvres has fewer restrictions, such as not restricting a specific orbit of target satellite, such as some methods only applicable to targets in GEO [39], or a specific way of manoeuvre, such as manoeuvring at perigee or apogee in the direction of velocity [32].

In addition, compared with the inertial orbital angular momentum in the geocentric coordinate system, the relative angular momentum in the coordinate system defined by Eq. (6) is more sensitive to manoeuvres. The reasons for this are analysed as follows.

The satellite carries limited energy, and thus the impulse of satellite manoeuvres is small [13, 40], resulting in a very small speed variation in a short time after the manoeuvre. However, the velocities of low Earth orbiting (LEO) satellite are on the order of 7.5 km/s. Therefore, the variation in the inertial position and velocity of the satellite in a short time after a manoeuvre is very small compared with its initial position and velocity before the manoeuvre. The angular momentum in a geocentric coordinate system consists of the position and velocity relative to the Earth's centre, which makes it difficult to identify the variation in the angular momentum within the noise. However, based on the assumption mentioned in the abstract that the two spacecraft are in high-altitude orbits and the relative range between them is far shorter than their geocentric distance, if the chaser satellite is taken as the reference point, the relative angular momentum in this coordinate system consists of the relative position and relative velocity, which greatly reduces the gap between the variation and the initial relative velocity. Therefore, the risk of the variation in the relative angular momentum being submerged by noise can be effectively reduced.

4. Manoeuvre detection algorithm

If the resultant force acting upon the target satellite does not point to the sensing satellite (the origin of the LVLH reference system), its relative angular momentum will change as follows [41]:

$$\frac{d\mathbf{h}_{rel}}{dt} = \boldsymbol{\tau} \quad (7)$$

where $\boldsymbol{\tau}$ is the unit mass moment on the target satellite relative to the COM of the chaser satellite.

When satellites are flying in free motion and the target satellite does not execute a manoeuvre, $\boldsymbol{\tau}$ is only provided by inertial forces, gravity and related perturbation forces. As a result, the change in $\boldsymbol{\tau}$ is very gentle, i.e., the change in \mathbf{h}_{rel} is continuous during the coasting flight. On contrary, if there is a sudden change in \mathbf{h}_{rel} , there must be a thrust or collision force put on the target. Therefore, when the orbit of the target changes, \mathbf{h}_{rel} will exhibit a sudden change, which can be naturally used to check the manoeuvre and determine the manoeuvre epoch.

However, it is difficult to use the individual time point information to determine the true single mutation point because the fluctuating local information value caused by the measurement is very likely to be identified as the true mutation point. Therefore, we aim to use more information to characterize the data and make decisions to reduce this possibility. According to Eq. (19), the information segments before the mutation point maintain the characteristics of continuous change, and they have a high correlation. However, when a certain information segment contains the mutation point, its trend changes, and thus the correlations between the information segments containing the mutation point information and all the previous information segments are very low. Using this phenomenon, we can divide the information into two types of segments with different characteristics: the information segments before the mutation

point and the information segments containing the mutation point. For example, Fig. 4 shows a group of virtual data containing a mutation point. The data before and after the mutation point satisfy Gaussian distributions, and a, b, c, and d are information segments of four sequential sliding windows with equal widths. In Fig. 4, we can see that although some local trends (trends of any number of sequential points, but the number is far less than the total) of a, b, and c are different owing to noise, the overall trends are almost the same, i.e., a, b, and c have a high correlation. However, the overall trend of d is very different from that of a, b, and c (i.e., the correlation is very low). Therefore, we can divide information segment d into a different category from that of information segments a, b, and c.

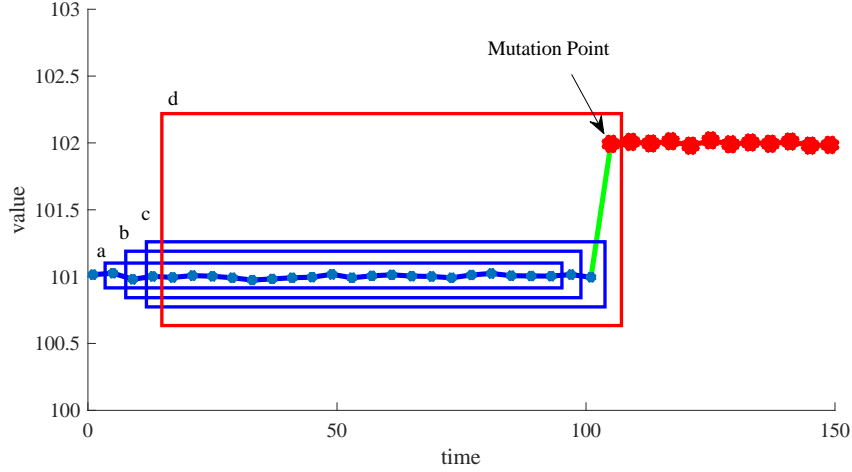


Figure 4: Illustration of sliding windows

Therefore, we can transform the problem of finding a single mutation point into that of finding an information segment including the mutation point; therefore, the concept of the correlation coefficient is introduced in this study. The correlation coefficient is a quantity that reflects the degree of correlation between variables. For example, for variables X and Y , the correlation coefficient is calculated as follows:

$$\rho_{XY} = r(X, Y) = \frac{\text{Cov}(X, Y)}{\sqrt{\text{Var}[X] \times \text{Var}[Y]}} \quad (8)$$

where $\text{Cov}(X, Y)$ is the covariance of X and Y , $\text{Var}[X]$ is the variance of X , and $\text{Var}[Y]$ is the variance of Y . The correlation coefficient, $\rho_{XY} \in [-1, 1]$, reflects the correlation between X and Y . The greater the value of $|\rho_{XY}|$, the higher the degree of correlation; the smaller the value of $|\rho_{XY}|$, the lower the degree of correlation.

Based on the characteristics of the correlation coefficient mentioned above, a simulated mutation array is established in this study. By calculating the correlation coefficients between each information segment of \mathbf{h}_{rel} and the simulated mutation array, the information segments before the mutation point can be distinguished from the information segments containing the information after the mutation point. Thus, the information segment containing the mutation information can be identified to determine the manoeuvre point. The specific calculation steps are described below.

Firstly, $\mathbf{h}_{simulated}$, an N -width sliding window made of an array of numbers, is defined to simulate the sudden change in the data. It is noticed that the setting of $\mathbf{h}_{simulated}$ is not unique. The requirement for setting $\mathbf{h}_{simulated}$ is that the trend of $\mathbf{h}_{simulated}$ is obviously different from the gentle change trend of \mathbf{h} when no manoeuvres (as mentioned after Eq. 19), and is as similar as the rapid change trend of \mathbf{h} after manoeuvres. Therefore, in fact, any group of arrays showing rapid changes can be set as $\mathbf{h}_{simulated}$, but it should be noted that when setting different $\mathbf{h}_{simulated}$, $\rho_{threshold}$ will be different (the definition of $\rho_{threshold}$ will be given later).

Then, each series of the three axes components of the relative angular momentum in the sliding window can be used to calculate the correlation coefficient with the simulated mutation array $\mathbf{h}_{simulated}$ as follows

$$\begin{cases} |\rho_{h_x(i)}| = \frac{|\text{Cov}(\mathbf{h}_{simulated}, \mathbf{h}_{X,window})|}{\sqrt{\text{Var}[\mathbf{h}_{simulated}] \times \text{Var}[\mathbf{h}_{X,window}]}} \\ |\rho_{h_y(i)}| = \frac{|\text{Cov}(\mathbf{h}_{simulated}, \mathbf{h}_{Y,window})|}{\sqrt{\text{Var}[\mathbf{h}_{simulated}] \times \text{Var}[\mathbf{h}_{Y,window}]}} \\ |\rho_{h_z(i)}| = \frac{|\text{Cov}(\mathbf{h}_{simulated}, \mathbf{h}_{Z,window})|}{\sqrt{\text{Var}[\mathbf{h}_{simulated}] \times \text{Var}[\mathbf{h}_{Z,window}]}} \end{cases} \quad (9)$$

where $\mathbf{h}_{X,window}$, $\mathbf{h}_{Y,window}$ and $\mathbf{h}_{Z,window}$ are the components of the estimate relative angular momentum in the sliding window.

Finally, the absolute values of the correlation coefficients, i.e. $|\rho_{h_{x/y/z}(i)}|$ (short for $|\rho_{h_x(i)}|$, $|\rho_{h_y(i)}|$ and $|\rho_{h_z(i)}|$) are used to compare with a designed threshold to determine the manoeuvre. In detail, if $|\rho_{h_{x/y/z}(i)}| > |\rho|_{threshold}$ is satisfied, the manoeuvre is deduced; on opposite, it infers no manoeuvre. Since the measurements are continuously obtained, the above steps can be repeated. Moreover, the threshold $|\rho|_{threshold}$ is defined as the maximum of $|\rho_{h_{x/y/z}(i)}|$ when the target does not manoeuvre in a large number of simulation experiments, which changes corresponding to specific $\mathbf{h}_{simulated}$.

5. Numerical simulations

To verify the effectiveness of the proposed method, a standard Monte Carlo simulation system with two-body dynamics is created to model the dynamics of the orbital manoeuvre detection. As this study is focused on orbit manoeuvre detection, the attitude of the satellite is not discussed as it is directly assumed the attitude of the chaser satellite keeps constant. Additionally, the effects of perturbations (J2 and higher-order gravity terms), vehicle mass and geometry (aerodynamic drag and solar radial pressure), and specific instrument error model structures is beyond the scope of this study as well.

Then, the truth models in the geocentric inertial frame for two spacecraft under two-body assumption can be given as follows

$$\begin{aligned} \dot{\mathbf{R}}_c &= \mathbf{V}_c & \dot{\mathbf{R}}_t &= \mathbf{V}_t \\ \dot{\mathbf{V}}_c &= -\frac{\mu}{|\mathbf{R}_c|^3} \mathbf{R}_c, & \dot{\mathbf{V}}_t &= -\frac{\mu}{|\mathbf{R}_t|^3} \mathbf{R}_t \end{aligned} \quad (10)$$

where μ is the standard gravity constant, $\mathbf{R}_c \in \mathbb{R}^3$ and $\mathbf{V}_c \in \mathbb{R}^3$ are the position and velocity of chaser satellite in the geocentric inertial frame, respectively, $\mathbf{R}_t \in \mathbb{R}^3$ and $\mathbf{V}_t \in \mathbb{R}^3$ are the position and velocity of target satellite in the geocentric inertial frame, respectively.

According to the measurement model in Eq. (5), the state of the target relative to the chaser satellite is obtained

$$\begin{aligned} \mathbf{r}_{rel} &= C_e^{lvlh} (\mathbf{R}_t - \mathbf{R}_c) \\ \mathbf{v}_{rel} &= C_e^{lvlh} (\mathbf{V}_t - \mathbf{V}_c) - C_e^{lvlh} [\boldsymbol{\omega} \times] (\mathbf{R}_t - \mathbf{R}_c) \end{aligned} \quad (11)$$

where is $\boldsymbol{\omega}$ the chaser satellite's inertial angular velocity vector, $[\times]$ denotes the cross-product operator, C_e^{lvlh} is the direction cosine matrix from geocentric inertial frame to LVLH frame which can be calculated from the orbit position and velocity vector. Finally, the true measurements are calculated from the true relative state and the camera offset as shown in Eq. (5).

5.1 Error models

It is assumed the attitude measurement error of the sensor satellite is made up of bias and Gaussian white noise. The bias for attitude is set to 0.001 rad/axis (X-axis, Y-axis and Z-axis) while the standard deviation of the white noise is set to 0.001 rad/axis (X-axis, Y-axis and Z-axis).

Meanwhile, as stated in Section 2.3, the line-of-sight angles measurement error is assumed to be Gaussian noise. Two values of the standard deviation of the LOS angles measurement noise are studied, i.e. $\sigma_{\text{cam}} = 3 \times 10^{-4}$ rad/axis or $\sigma_{\text{cam}} = 3 \times 10^{-5}$ rad/axis (azimuth-axis and elevation-axis). The specific selection of the sensor is described in a subsequent section.

5.2 Reference mission and trajectory

It is assumed the chaser satellite is orbiting near Geostationary Earth Orbit (GEO) as shown in Tab. 1, while two types of target's orbit are set in terms of the relative range. The first type is long-range case that is beyond one hundred kilometers, as shown in Table 2, where the target orbit is set by the differences with the parameters shown in Tab. 1 (The eccentricity and right ascension are the same). The second type is kilometers level close-range case as shown in Tab. 3, where four classical motion including V-bar Stationary, Co-elliptic, Football and Oscillating orbit for inspection is presented.

Table 1: Initial orbit parameters of the chaser satellite

Semi-major axis	Eccentricity	Inclination	Ascending node	Argument of perigee	True anomaly
42 278.14 km	0.001	0°	0°	0°	200°

Table 2: Type 1: Initial relative orbit parameters of long-range target relative to the chaser satellite

	Altitude difference	Phase difference	Inclination difference	Relative distance
Target 1	20 km	0.15°	0°	112.512 km
Target 2	70 km	0.30°	0°	232.365 km
Target 3	20 km	0.15°	0.5°	169.431 km

Table 3: Type 2: Initial relative orbit parameters of close-range target relative to the chaser satellite

	Eccentricity			Inclination		
	X	Y	Z	X	Y	Z
V-bar	1 000	0	0	0	0	0
Co-elliptic	1 000	0	0	0	0	0.563 42
Football	1 000	0	-100	-0.169 26	0	0
Oscillating	1 000	0	0	0	-0.112 84	0

5.3 Computation models for estimation of the error

Since the LOS angles and camera offset are measured values with noise, Monte Carlo simulation is employed to evaluate the accuracy of these statistics. The error models presented in Section 5.1 are then used to generate a set of

measurements that are processed by the proposed algorithm to determine the maneuver for the i -th Monte Carlo sample.

To verify the validity and test the performance of the proposed algorithm, two parameters will be checked. The first one is accuracy of the maneuver determination, defined by the true positive rate in all of the Monte Carlo runs

$$P_m = \frac{m}{n} \times 100\% \quad (12)$$

where m represents number of the correct determination cases while n is the number of Monte Carlo runs. 200 runs are selected for the Monte Carlo simulations which can roughly lead to 90% confidence [42](Buckland, 1984).

The second one is the estimate error of the maneuver epoch for the determined cases, defined as follows

$$e_{true} = \frac{1}{n} \sum_{j=1}^n |t_e - t_r| \quad (13)$$

where t_e is estimated maneuver epoch and t_r is the reference one for the j -th Monte Carlo sample.

6. Performance analysis

6.1 Settings of key parameters

As the calculation steps mentioned in Section 4, $\mathbf{h}_{simulated}$ and $\rho_{threshold}$ need to be set at first.

As mentioned in the steps, $\mathbf{h}_{simulated}$ is not unique, but after a large number of experimental attempts, it is found that the growth section of the quadratic parabola meets the requirements well, so this paper sets $\mathbf{h}_{simulated}$ as follows:

$$\mathbf{h}_{simulated} = [1^2, 2^2, 3^2, \dots, N^2] \quad (14)$$

And $\rho_{threshold}$ is set to 0.989 in this paper after 200 Monte Carlo runs corresponding to the setting of $\mathbf{h}_{simulated}$ in Eq. 26.

6.2 Results of long-range cases

6.2.1 Maneuver detection error and the true positive rate

As discussed in previous section, the estimation of the relative angular momentum is polluted by the sensor noise. Thus, an appropriate width sliding window is quite important for matching with the pre-defined mutation simulation array during the detection. Too small or too large of a sliding window will affect the ability of the window containing data to reflect the overall characteristics of the actual inspection quantity. To test the performance of different width windows, the following simulation is conducted: Target 1 is selected to test, $\sigma_{cam} = 3 \times 10^{-4}$ rad/axis, and a random directed 1 m/s impulse is executed at $t = 3\ 000$ s.

The results of 20 runs are shown in Fig. 5 to present the distribution of maneuver detection errors in terms of different sliding widths. It can be seen that when the width of sliding window is too small, the detection errors are relatively large. In these cases, the false positive rate is high because the estimation data in the narrow window cannot reflect the overall actual characteristics of the trend. As the width increases, the false positive rate significantly reduces. According to the performance shown in Fig. 5, a sliding window with 50 widths is a good choice for the detection, which will be used for the subsequent simulations.

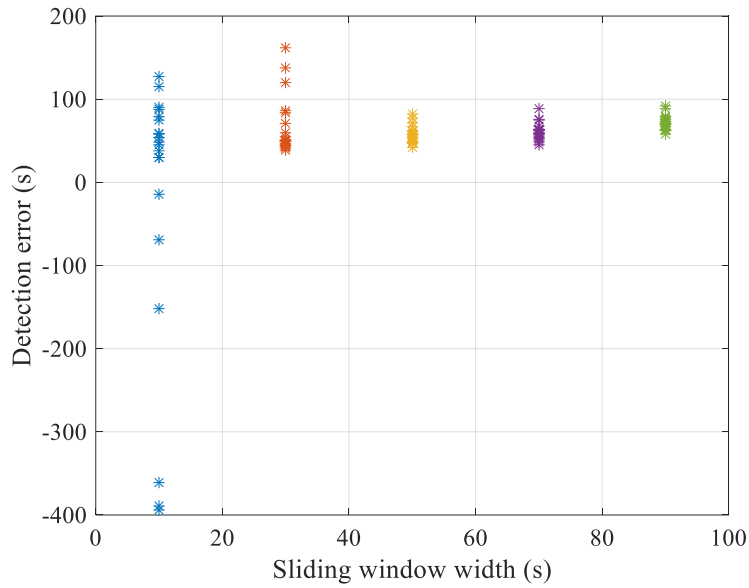
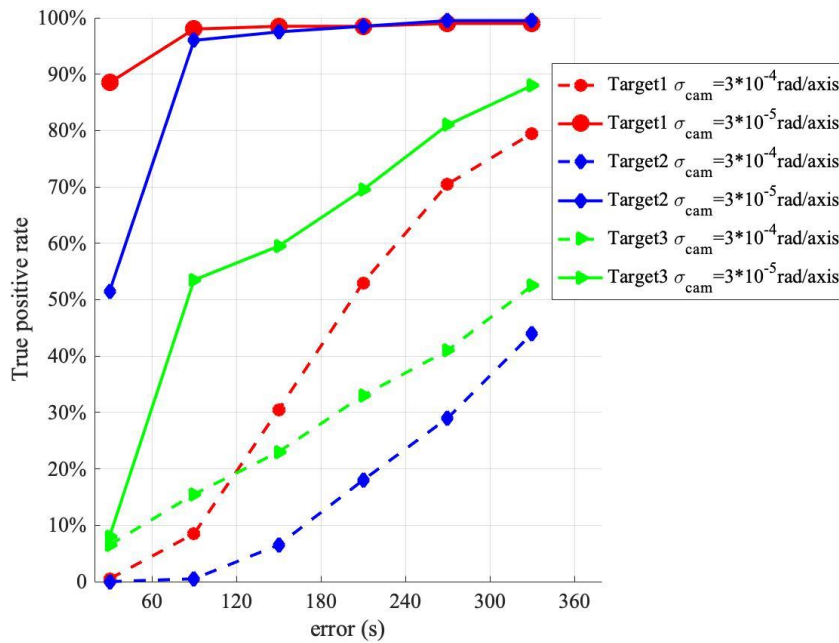
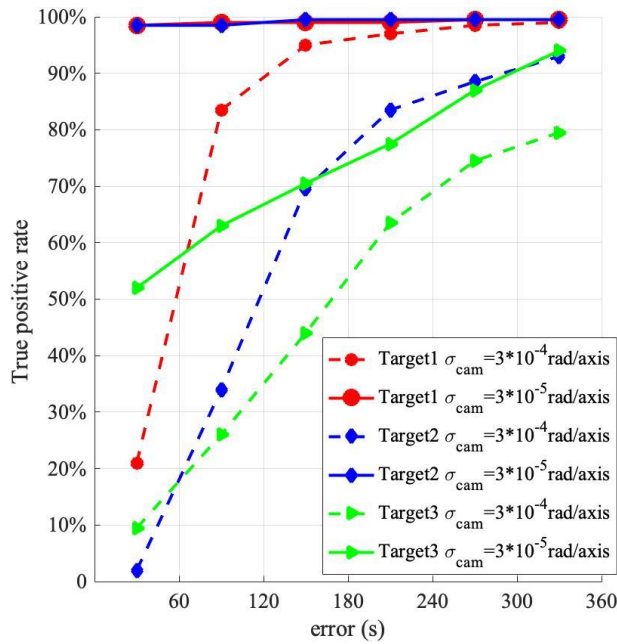
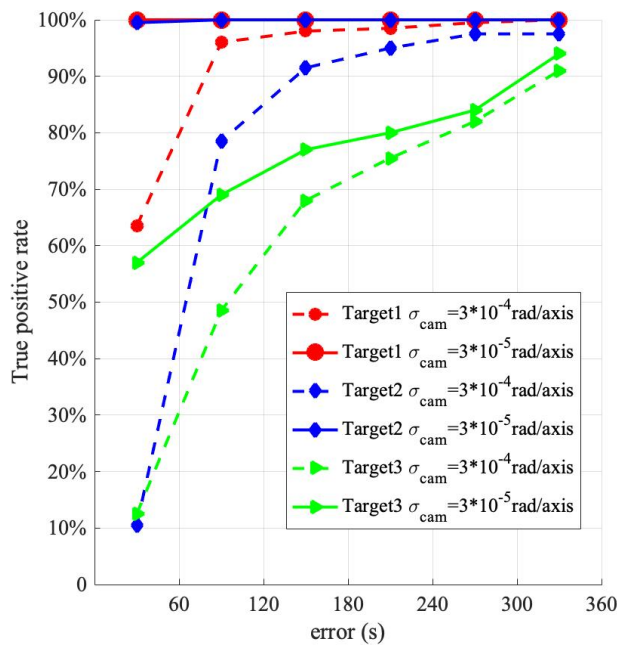


Figure 5: Detection error distribution under different window widths

Next, the sensitivities of the proposed algorithm to the accuracy of the optical sensor, magnitude of the maneuver, and different relative orbit types are checked in the following simulations. 200 Monte Carlo runs are conducted for each case, where the maneuver is executed at $t = 3\,000$ s. The simulation results are shown in Figs. 6-8 while the average errors of 200 runs are presented in Tab. 4. The sixth points from left to right on the curve represent the probability that the detection error is less than 60 s, 120 s, 180 s, 240 s, 300 s, and 360 s, respectively.

Figure 6: True positive rate of detection with $\Delta V = 0.2$ m/s

Figure 7: True positive rate of detection with $\Delta V = 0.6 \text{ m/s}$ Figure 8: True positive rate of detection with $\Delta V = 1.0 \text{ m/s}$

By comparing the detection results for the same target with different observation sensor accuracies in Figs. 6-8, it can be concluded that the detection performance is improved with higher detection accuracy. Taking Target 1 in Fig. 12 as an example, the red solid line is the detection result under the high-precision sensor, and the red dotted line is the detection result under the low-precision sensor. It can be seen in Fig. 12 that the distance between the two curves is large initially and then decreases. This shows that with the high-precision sensor, the detection error has a greater probability of being concentrated in a place with a small value, and the overall error is smaller.

Figs. 6-8 also indicate the maneuver magnitude has significant influence on the performance. For small maneuvers (e.g., 0.2 m/s), the detection with the low-precision sensor is less effective, but it is more effective with the high-precision sensor. With the high-precision sensor, the detections of coplanar Target 1 and Target 2 are better than that of the heterogeneous Target 3. The true positive rate of Target 1 with a detection error of less than 60 s is 88.5% and that of less than 120 s is 98%. The true positive rate of Target 2 with a detection error of less than 120 s is 96%. The detection error of Target 3 is greater than that of the coplanar targets overall; however, for a detection error of less than 360 s, the true positive rate is 88%. When the maneuver magnitude is 0.6 m/s, the probability that the detection error

of Target 1 and Target 2 is less than 60 s reaches 98.5%, and the true positive rate for a detection error of Target 3 of less than 360 s increases to 94%. When the maneuver magnitude reaches 1.0 m/s, the probability that the detection errors of Target 1 and Target 2 are less than 60 s is close to 100%. This shows that the method proposed in this study requires a high-precision measurement sensor for small maneuvers; otherwise, the detection performance will be reduced or lost. For large maneuver magnitude cases, the detection error of the high-precision measurement sensor is smaller overall. However, if the magnitude of the detection error is not considered, but only whether the target orbit maneuver is detected, there is little difference in the detection true positive rate. In this case, a low-precision measurement sensor with a lower cost can be selected.

Additionally, the results show that the detection performance for targets in coplanar orbits such as Target 1 and Target 2 is better than for targets in non-coplanar orbits, such as Target 3. The detection errors for targets in coplanar orbits have a greater probability than those of targets in non-coplanar orbits to fall in range with small values, so the overall errors for targets in coplanar orbits smaller. Moreover, comparison of Target 1 and Target 2 shows that among the coplanar targets, the performance for the closer targets is better, the reason of which is that the orbit determination of closer targets is more accurate and stable, thus the variation in characterization, i.e. $\mathbf{h}_{simulated}$ caused by orbit maneuvers is more obvious.

The above analysis demonstrates that the distance and coplanarity can impact the detection performance. Comparing the results for Target 2, which is more distant but coplanar, with those for Target 3, which is closer but not coplanar, indicates the negative impact of not being coplanar is greater than that of the larger distance.

Table 4: Average detection errors

Target	σ_{cam}	$\Delta V = 0.2 \text{ m/s}$	$\Delta V = 0.6 \text{ m/s}$	$\Delta V = 1.0 \text{ m/s}$
Target 1	$3 \times 10^{-4} \text{ rad/axis}$	238.00 s	85.90 s	58.05 s
	$3 \times 10^{-5} \text{ rad/axis}$	41.80 s	36.90 s	35.45 s
Target 2	$3 \times 10^{-4} \text{ rad/axis}$	262.91 s	148.67 s	89.85 s
	$3 \times 10^{-5} \text{ rad/axis}$	55.05 s	38.80 s	37.70 s
Target 3	$3 \times 10^{-4} \text{ rad/axis}$	230.23 s	122.13 s	160.89 s
	$3 \times 10^{-5} \text{ rad/axis}$	129.72 s	59.10 s	130.67 s

Table 4 shows the average detection errors for different targets with different settings of sensors. As expected, errors were smaller with high-precision measurement sensors. As increase of ΔV , the errors reduce, expect for Target 3. The reason is that when selecting $\mathbf{h}_{simulated}$ and $\rho_{threshold}$, we decide to try to detect all maneuvers as possible sacrificing the size of errors, so $\mathbf{h}_{simulated}$ may not be most suitable considering the size of errors when ΔV is a certain value. And this also explains why some other expected phenomena, such as obvious differences in average detection errors between targets in different distance or between targets in coplanar orbits and in non-coplanar orbits, do not appear in Table 5.

Further, a comparison of performance between the proposed approach in this paper and the algorithm in studies by Liu et al. [33] and Wang et al. [34] is conducted. Liu et al. [33] present a maneuver detection scheme based on space-based LOS angle measurements. To make fair comparison, a magnitude of maneuver impulse, i.e. 1 m/s impulse as same as the one used in study by Liu et al., is executed to the Target 1. The detection true positive rate by using Liu's scheme is approximately 90%, which is less than the result by the proposed algorithm in this study.

Wang et al. [34] developed a maneuver detecting method based on space-based Lidar, which provides excellent ranging performance (the standard deviation of the noise is 0.05 m). When the standard deviation of the noise increases to 0.5 m, the Wang's method maintains excellent detection capability. However, when it comes up to 5 m, the detection performance greatly reduces, and if the standard deviation of the noise comes up to 8 m or even larger, the method would fail. On the contrary, the proposed method in this study works well in the case that the relative position uncertainty is more than 8 m when $\sigma_{cam} = 3 \times 10^{-5} \text{ rad/axis}$.

6.2.2 Double single-impulse maneuver detection and tracking

To demonstrate the multiple-maneuver tracking ability of the proposed method, the following simulations based on Target 1 are conducted. The first maneuver, i.e. random directed impulse with magnitude of 0.4 m/s is executed at $t = 2500 \text{ s}$, and the second maneuver, i.e. random directed impulse with magnitude of 1 m/s is executed at $t = 5000 \text{ s}$.

Moreover, σ_{cam} is set to 3×10^{-4} rad/axis. The filter for the estimation of relative position and velocity is set to be restarted after a maneuver is determined.

The results of the estimate error of the relative position and velocity are shown in Figs. 9-10. It can be seen that both the maneuvers are detected, and the detection error is quite small. In detail, the first maneuver detection result is $t = 2579$ s with an error of 79 s, and the second detection result is $t = 5058$ s with an error of 58 s. After filter being restarted, the estimation error is going to converge and then keep convergent, as indicated by the red curves. In contrast, the blue curves presented the errors without the proposed method are divergent after maneuvers.

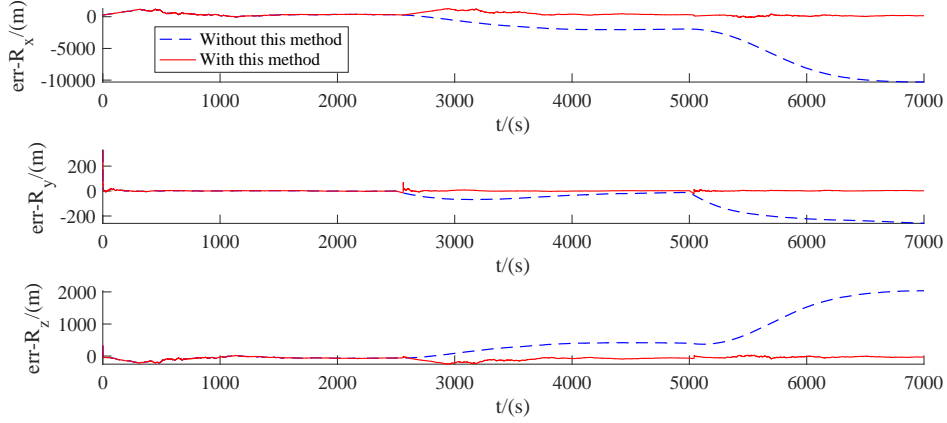


Figure 9: Relative position estimation error of Target 1

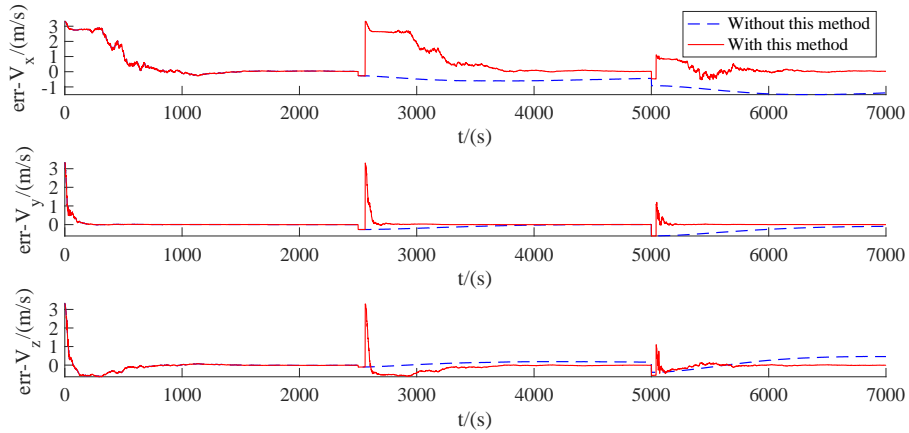


Figure 10: Relative velocity estimation error of Target 1

6.2.3 Results of close-range cases

The application in the close-range cases is tested in this section. A random pointed impulse maneuver with 0.1m/s magnitude is executed at $t = 600$ s and $\sigma_{\text{cam}} = 3 \times 10^{-4}$ rad/axis is selected for the simulation. The results based on 200 Monte Carlo runs are summarized in Tab. 5, where the initial relative orbit is randomly selected for each runs in the four type shown in Tab. 3.

Table 5: Detection true positive rate for close-range case

	Error < 30 s	Error < 60 s	Error < 90 s	Error < 120 s
$\Delta V = 0.1$ m/s	93.5%	98.5%	98.5%	98.5%

As can be seen from Tab. 5, the maneuver of 93.5% of the runs is successfully estimated within 30s after maneuver, and 98.5% is estimated within 60s. However, the true positive rate does not change when error is greater than 60s. It indicates that the left 1.5% runs did not be detected because of the sensor noise.

The continuous tracking performance for a close-range target initialized in V-bar stationary orbit (which is considered as the most disadvantageous trajectory for angles-only navigation) is tested. There are two randomly directed impulses are executed at $t = 500\text{s}$ and $t = 700\text{s}$ with the magnitude of 0.1m/s and 1m/s respectively. The results are shown in Figs. 11-12, where the red curves present the estimate errors with the proposed method and the blue curves present the errors without the proposed method. It can be seen that the maneuvers are detected and the estimate error is convergent after the restarting of the filter when each maneuver is detected. The errors of the two detection results are 23 s and 29 s, respectively.

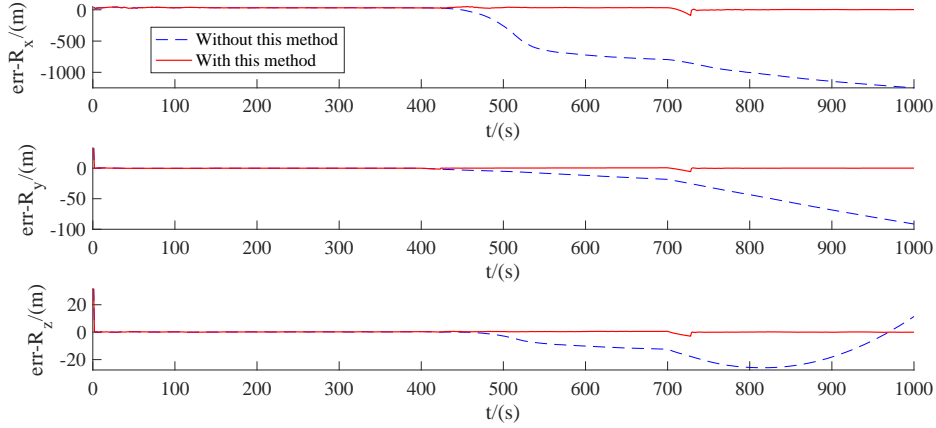


Figure 11: Relative position estimation error for a close-range target

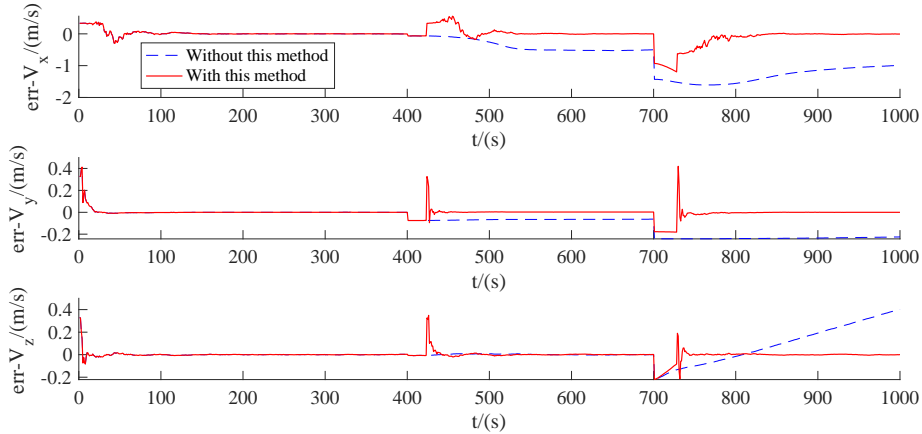


Figure 12: Relative velocity estimation error for a close-range target

7. Conclusion

In this study, a novel space-based passive orbital maneuver detection algorithm for a non-cooperative space target is developed, where the concept of relative angular momentum is introduced to characterize the maneuver. A standard Monte Carlo simulation system with two-body dynamics was created to validate the proposed algorithm and evaluate the performance in the context of near GEO orbit space. The accuracy of the detection algorithm was determined and presented for a variety of parameters and trajectories. When $\sigma_{\text{cam}} = 3 \times 10^{-5}$ rad / axis, the true positive rates approach 100%, much better than when $\sigma_{\text{cam}} = 3 \times 10^{-4}$ rad / axis. The average detection errors is greater when the orbit of the chaser satellite and the target satellite are not in the same plane, but no obvious difference in true positive rate. As expected, the algorithm worked better for close-range cases than for cases where the target was kilometers away. Surprisingly, the detection algorithm worked well for the long-range cases that hundreds of kilometers away while the magnitude of the maneuver impulse is as small as to 0.2 m/s. In future, the detection algorithm for continuous low thrust maneuver will be studied.

Acknowledgements

This work is partially supported by the National Natural Science Foundation of China (12272168, 11802119, 42271448).

References

- [1] MARK C P, KAMATH S. 2019. Review of active space debris removal methods. *J. Space Policy*. 47: 194-206.
- [2] HAKIMA H, BAZZOCCHI M, EMAMI M R. 2018. A deorbiter CubeSat for active orbital debris removal. *J. Advances in Space Research*. 61(9): 2377-2392.
- [3] HAKIMA H, EMAMI M R. 2018. Assessment of active methods for removal of LEO debris. *J. Acta Astronautica*. 144: 225-243.
- [4] SURDI S A. 2020. Space situational awareness through blockchain technology. *J. Journal of Space Safety Engineering*. 7(3): 295-301.
- [5] CHEN Y T, TIAN G Q, GUO J Y, et al. 2021. Task planning for multiple-satellite space- situational-awareness systems. *J. Aerospace*. 8(3): 73.
- [6] Miller, G. D. (2021). Deterrence by Debris: The Downside to Cleaning up Space, *Space Policy*, 58.
- [7] Serfontein, Z., Kingston, J., Hobbs, S., Holbrough, I. E., & Beck, J. C. 2021. Drag augmentation systems for space debris mitigation. *J. Acta Astronautica*. 188:278-288.
- [8] Xu, W. D. 2021. Space Competition and Cooperation: Current Space Security and Chinese Responsive Approaches. *J. Space Debris Research*. 21(01): 18-25.
- [9] Zhang, S. J., Duan, C. Y., & Su, H. 2015. Natural-artificial Space Security Threats and Their Mitigation Strategies. *J. Journal of Command and Control*. 1(01): 92-98.
- [10] Chen, Y., Wei, G. N., Tang, S. Y., & Kang, Z. Y. 2021. Global Space Security Situation Analysis and Development Proposal. *J. AIR & SPACE DEFENSE*. 4(03): 99-104.
- [11] Long, K., Zhu, Q. C., Chen, X., & Ma, N. 2021. Invited Paper: Trump administration's Defense Space Strategy adjustment: motivations, characteristics and implications. *J. National Defense Technology*. 42(04): 76-84.
- [12] Hao, Y. N., Chen, J., Zhu, B., & Wang, Y. Y. 2019. Current situation and trend of ground-based space situational awareness system of U.S. Army. *J. Defense Science & Technology Industry*. 225(03): 32-35.
- [13] Cui, H. Z., Liu, W. L., Tang, G. S., Song, B. Y., & Ge, M. R. 2016. Different thrust maneuvers detection of uncooperative space objects. *J. Journal of Astronautics*. 37(03): 253-261.
- [14] Bergmann, C. M., Zollo, A., Herzog, J., & Schildknecht, T. 2021. Integrated Maneuver Detection and Estimation Using Nonlinear Kalman Filters During Orbit Determination of Satellites. In: *8th European Conference on Space Debris*.
- [15] Liu, Y., Zhao, H., Liu, C., Cao, J., & Wang, J. 2020. Maneuver detection and tracking of a space target based on a joint filter model. *J. Asian Journal of Control*. 23(3): 1441-1453.
- [16] Yang, Z., & Li, Z. 2015. Research the status of space based optical imaging observation for resident space objects. *J. Foreign Electronic Measurement Technology*. 34(10): 58-61+78.
- [17] Busch, W. F. 2018. Enhancing SSA capabilities to ensure the security of all space systems: the French approach. In: *3th Military Space Situational Awareness Conference*. London, UK, April 25-26.
- [18] Song, B. 2015. Development of U.S. Space-based Space Situational Awareness System. *J. Space International* (12):8.
- [19] Gong, J. G., Ning Y., & Lyu, N. 2021. Development and Enlightenment of Space Based Situational Awareness Technology for High Orbit in the United States. *J. Aerospace Control and Application*. 47(01): 1-7.
- [20] Fan, Z. H., Cai, Y. X., & Li, F. Z. 2019. Study on Development of American Space-based Situational Awareness Technology for GEO Objects. *J. Spacecraft Engineering*. 28(06): 87-95.
- [21] Gong, B. C., Li, W. D., Li, S., Ma, W. H., & Zheng, L. L. 2018. Angles-only initial relative orbit determination algorithm for non-cooperative spacecraft proximity operations. *J. Astrodynamics*. 2: 217-231.
- [22] Liu, Z. X., Sun, Y. R., Zeng, Q. H., & Zhao, K. D. 2021. Relative Navigation Algorithm Based on DG-IEKF Under the Range and Angle Information. *J. Navigation and Control*. 20(03): 34-43.
- [23] Du, R. H., Zhang, X., & Liao, W. H. 2021. Fast initial relative orbit determination method of angles-only relative navigation. *J. Systems Engineering and Electronics*. 43(04): 1057-1068.
- [24] Du, R. H., Zhang, X., Wang, N., Wang, L., & Zhang, X. X. 2021. Research on Autonomous Detection and Tracking Method for Rendezvous and Proximity of an Uncooperative Target. *J. Journal of Astronautics*. 42(05): 621-633.
- [25] Jia, B., Blasch, E., Pham, K.D., Dan, S., & Chen, G. 2015. Space object tracking and maneuver detection via interacting multiple model cubature Kalman filters. In: *IEEE Aerospace Conference Proceedings*.

- [26] Li, W. F., & Duan, X. J. 2015. Detection and Analysis of Orbital Anomalies Based on EMD. In: *the first China Aerospace Safety Conference*.
- [27] Li, Y., Han, Z. H., & Tian, W. 2017. Detecting Orbit Transferring of Geostationary satellites in the EMD Domain Using the adaptive noise threshold. In: *13th Annual Conference on satellite communications*.
- [28] SPURBECK J, JAH, M K, KUCHARSKI D, et al. 2021. Near real time satellite event detection, characterization, and operational assessment via the exploitation of remote photoacoustic signatures. *J. The Journal of the Astronautical Sciences*. 68(1): 197-224
- [29] BAI X, LIAO C, PAN X, XU M. 2019. Mining two-line element data to detect orbital maneuver for satellite. *J. IEEE Access*. 7: 129537-129550.
- [30] YU S X, WANG X, ZHU T L. 2021. Maneuver detection methods for space objects based on dynamical model. *J Advances in Space Research*. 68(1): 71-84.
- [31] Yu, D.T., Wang, H., You, Y., & Bai, X. Z. 2013. A new in-plane maneuver detection method for incomplete orbit information of LEO spacecraft. *J. Journal of Astronautics*. 34(03): 314-319.
- [32] Huang, J., Hu, W. D., & Zhang, L. F. 2013. Maneuver Detection of Space Object for Space Surveillance. *J. Esa Special Publication*.
- [33] Liu, L., Cao, J. F., & Liu, Y. 2018. WFMHT Method of Orbit Maneuver Detection Based on Space-Based Bearing-Only Measurement. *J. Journal of Northwestern Polytechnical University*. 36(06):1185-1192.
- [34] Wang, Q. R., Zou, J. W., Wu, W. Z., & Chen, J. 2021. Orbital maneuver detection method of space target based on Neyman-Pearson criterion. *J. Chinese Space Science and Technology*. 41(02): 96-103.
- [35] FAN L H, TU R, ZHANG R, et al. 2022. An orbit maneuver detection method based on orbital elements for BeiDou GEO and IGSO satellites. *J. Advances in Space Research*. 69(10): 3644-3654.
- [36] QIN Z W, HUANG G W, ZHANG Q, et al. 2021. The analysis and detection of orbit maneuvers for the BeiDou satellites based on orbital elements[J]. *J. Acta Geodaetica et Geophysica*. 2021, 56(3): 501-522.
- [37] Gong, B. C., Luo, J. J., Li, S., & Li, W. D. 2018. Observability criterion of angles-only navigation for spacecraft proximity operations. *J. Proceedings of the Institution of Mechanical Engineers, Part G: Journal of Aerospace Engineering*. 233(12): 4302-4315.
- [38] Yamanaka, K., & Ankersen, F. 2002. New state transition matrix for relative motion on an arbitrary elliptical orbit. *J Journal of Guidance Control & Dynamics*. 25(1): 60-66.
- [39] ROBERTS T G, LINARES R. 2020. Satellite repositioning maneuver detection in geosynchronous orbit using two-line element (TLE) data. In: *71st International Astronautical Congress*.
- [40] YAHYA N A, VARATHARAJOO R, HARITHUDDIN A S M, et al. 2022. Delta-V and ground metric investigations for responsive satellite formation flying. *J. Acta Astronautica*, 193: 20-34.
- [41] ROSE M E. 1995. Elementary theory of angular momentum. North Chelmsford: Courier Corporation.
- [42] Buckland, S. T. 1984. Monte Carlo Confidence Intervals. *J. Biometrics*. 40(3):811-817.